Towards the Validation of a Phase Field Model for Ni Coarsening in Solid Oxide Cells

M. Trini[a#], S. De Angelis[b*#], P. S. Jørgensen[c], P. V. Hendriksen[c], K. Thornton[d], M. Chen[c*]

[a] Fondazione Bruno Kessler, ARES – Applied Research on Energy systems, Via Sommarive 18, 38128, Trento, Italy

[b] Paul Scherrer Institut, Electrochemistry Laboratory, Forschungsstrasse 111, 5232 Villigen PSI, Switzerland

[c] Department of Energy Conversion and Storage, Technical University of Denmark, 2800 Kgs. Lyngby, Denmark

[d] Department of Material Science and Engineering, University of Michigan, Ann Arbor, Michigan 48109, USA

[#] Authors contributed equally to the manuscript.

Corresponding authors:

Ming Chen; Tel: +46 77 57 57; Fax: +46 77 58 58; E-mail address: minc@dtu.dk (Ming Chen)

Salvatore De Angelis; Tel: +41 56 310 53 50; E-mail address: salvatore.de-angelis@psi.ch (Salvatore De Angelis)

Other authors:

Martina Trini: E-mail address: mtrini@fbk.eu

Peter Stanley Jørgensen: E-Mail address: psjq@dtu.dk

Peter Vang Hendriksen: E-Mail address: pvhe@dtu.dk

Katsuyo Thornton: E-mail address: kthorn@umich.edu

Abstract

Ni coarsening in the Ni/yttria-stabilized zirconia (YSZ) fuel electrode of solid oxide cells (SOCs) is a major cause of long-term performance degradation. Phase-field modeling is a powerful tool for studying Ni coarsening in the complex 3D structures of SOC fuel electrodes. In this work, we present a study aimed at validating a phase-field model, comparing simulation results with time-dependent ex-situ tomographic data. Three equilibrium Ni/YSZ contact angles are examined: 97°, 120°, and 150°. Simulated microstructures are characterized through quantities such as the Ni mean radius, triple-phase boundaries, and interface shape distribution. The phase-field model reproduces the improved pore connectivity in the first stage of Ni coarsening observed in the tomography data. This model also indicates that the contact angle plays a key role in the microstructural evolution during Ni coarsening, and the best match to the experiment was obtained with the equilibrium contact angle of 120º, close to a measured value in literature. Finally, the limitations of the model are discussed.

1. Introduction

Solid oxide cells (SOCs) are electrochemical devices used for converting between chemical energy and electrical energy [1, 2]. This technology is attractive due to its high efficiency, low cost of constituent materials, and the ability to operate with different hydrocarbons via internal reforming. Furthermore, SOCs can operate reversibly, storing energy as chemical fuel and producing electricity on demand, and therefore offer a technology for the integration of renewable intermittent energy sources into future energy systems.

Despite these advantages, several degradation phenomena impede the widespread commercialization of SOC technology. A SOC is composed of three layers: an oxygen electrode, a thin solid electrolyte, and a fuel electrode [1, 2]. State-of-the-art fuel electrodes are porous composite cermets fabricated by sintering nickel oxide (NiO) and yttria-stabilized zirconia (YSZ) together to form a complex 3D structure [2]. Prior to first use, NiO is reduced to Ni by feeding H_2 over the composite at an elevated

temperature (700 – 1000°C), resulting in a cermet rich in electrochemically active triple-phase boundaries (TPBs) between the gas, YSZ, and Ni. Among the degradation mechanisms, Ni coarsening has been suggested as a major cause of performance degradation [3-7]. Due to the SOC's high operating temperatures, Ni particles tend to coarsen, reducing the triple-phase boundaries and affecting the Ni and pore connectivity required for the transport of reactants, products, ions, and electrons [3-5]. Therefore, a deeper understanding of the mechanisms of Ni coarsening and their effects on the overall Ni/YSZ microstructure is crucial.

Elucidating the morphological evolution of a given Ni/YSZ cermet structure through accurate microstructural modeling will enable the prediction of performance degradation. The resulting insights may form a foundation for the design of the microstructure that would improve the lifetime of future fuel electrodes. In the past decade, Ni coarsening has been simulated using a variety of approaches, ranging from particle-size-distribution-based models [8-11] to fully resolved 3D models [12-16]. Ni particle growth has been described with power laws [8], diffusion-based models for two-particle coarsening [9, 10], and "charging capacitor models" [11]. However, these models are based on the assumption of spherical Ni particles and cannot fully capture the morphological changes occurring in the real 3D Ni/YSZ microstructures.

Phase-field modeling is a valuable tool for simulating Ni coarsening in SOCs. Using this approach, Davis et al. [16] simulated the evolution of the Ni/YSZ electrode microstructure digitally generated as randomly close-packed spherical particles. Moreover, both the artificial SOC microstructure evolution and electrochemical performance were simulated by Jiao and Lei [13, 17]. Three-dimensional reconstructions of real Ni/YSZ electrodes can be obtained by tomographic techniques [6, 7, 8, 12, 18-25] such as focused ion beam milling with scanning electron microscopy (FIB-SEM) [6, 12-14, 26-28] and X-ray nanotomography [8, 20-25]. Using this approach, Chen et al. [12] simulated the evolution of an experimentally obtained Ni/YSZ microstructure varying the Ni/YSZ interfacial energy, while Jiao et al. also included crystallographic information in their phase-field

simulations [13, 14]. However, a direct comparison between experimental and simulated microstructural changes is still lacking in the existing literature. To date, the comparisons have been limited to overall microstructural characteristics (e.g., the surface area per unit volume as well as the triple-phase boundary density) [12, 13, 15, 16].

In this paper, simulation results are compared with experimental data [25], where the evolution of the same microstructure is observed via time-resolved X-ray tomography. Morphological changes, in addition to the evolution of microstructure parameters, are directly compared with experimental results, providing a stringent test of the phase-field model.

2. Experimental

2.1 X-ray ex-situ tomographic ptychography

Details of the sample preparation and ex-situ tomography experiments were previously reported in Ref. [25]. The sample was prepared from a Ni/YSZ anode-supported SOC half-cell. Details of the cell fabrication can be found in Ref. [29]. The sample was extracted from the functional layer using precision polishing and FIB milling (CrossBeam X1540, *Zeiss*) to obtain a final cylindrical pillar ~14 µm in diameter and ~15 µm in height. The composition of the cell in its pristine state (before performing the annealing experiment) was 29 vol.% of Ni, 41 vol.% of YSZ, and 30 vol.% of porosity. These values change only marginally upon annealing (± ~1%), which is within the uncertainty of the image analysis.

The ptychographic tomography experiment was performed at the X12SA (cSAXS) beamline at the Swiss Light Source, Paul Scherrer Institut, Switzerland, using the instrumentation described in Ref. [30].

91 The sample was initially imaged in the pristine state and then characterized after three hours at 850°C
92 in a gas mixture of 4 % H_2 and 96 % N_2. The treatment was conducted in a small custom-made tube
93 furnace with a flow rate of 5 l/h. The ramping rate was 10°C/min for both heating and cooling [25].

94 *2.2 Segmentation, registration and microstructure quantification*

95 The acquired datasets were registered to the pristine dataset, which was first rotated to orient the
96 normal of the electrode-electrolyte interface to the x-axis, where positive direction points toward the
97 electrolyte. The registration was performed using points from the YSZ (assumed stationary), and a
98 rigid transformation was carried out by the iterative closest point method [31]. Subsequently, the 3D
99 datasets were segmented using a 2D histogram thresholding procedure, which involves the
100 determination of segmentation thresholds based on the intensity and the magnitude of the intensity
101 gradient [25].

102 Microstructures were quantitatively characterized by the average particle radius, interfacial areas, and
103 connectivity. The particle size distribution (PSD) was computed using the continuous particle size
104 distribution approach [26]. In addition, the connectivity of each phase network was analyzed by
105 labeling each unconnected region. More details on the methods for calculating these quantities are
106 described elsewhere [26, 32]. To accurately calculate interfacial curvatures required to compute the
107 interface shape distribution (ISD) [33], the Ni phase field was produced by a combination of diffusion
108 smoothing and evolution via level-set equation [34]. First, the segmented binary 3D image of Ni with
109 sharp interface, with cubic voxels of uniform size was smoothed with 30 steps of evolution using the
110 diffusion equation, with a grid size of 1 and a time step size of 0.1, which produced a Ni phase-field
111 with a gradual transition between 0 and 1 over the interface. This smoothing procedure was required
112 to increase the accuracy of the computed surface curvature from the experimental voxelated
113 structures. Second, the level-set distancing equation was used to produce a distance function across
114 approximately 8 points (4 points on each side) in the vicinity of interfaces by setting the maximum

of the function to be 6 times the grid spacing. All of these numerical parameters were adopted from Ref. [34], which provides the details of the method and extensive error analysis. The same procedure was applied for simulated microstructural data after it was binarized. A regular triangulated mesh was then generated for the interface using Interactive Data Language (IDL®) [33] for the level set at 0.5. To compute the interfacial areas, the areas of the polygons generated were summed. The mean and Gaussian curvatures were calculated on this grid using a level-set-method-based approach [34]. The results were then interpolated to the interface mesh [33], and the principal curvatures (κ_1 and κ_2) were calculated using the relationships $H = \frac{(\kappa_1+\kappa_2)}{2}$ and $K = \kappa_1\kappa_2$, where the convention $\kappa_2 \geq \kappa_1$ was taken. The probability distribution of the curvatures was then computed and is plotted in the ISD diagram presented in Sec. 4.4. Additionally, the contact angles were determined based on the same phase fields using the relationship $-\cos\theta_c = (\nabla\psi/|\nabla\psi|) \cdot (\nabla c/|\nabla c|)$ in the region where both $0.1 < \psi < 0.9$ and $0.1 < c < 0.9$, and the average value is reported in Sec. 4.1.

3. Phase-Field Modeling

3.1 Model formulation

The phase-field model is based on a diffuse interface description of multiphase systems, which is widely employed in simulating phase transformations and microstructural evolutions in multiphase materials [12, 35, 36]. In this model, the constituent phases of a multiphase system are described by one or more fields known as order parameters (OPs). The OPs assume a constant value in the bulk phases (typically 1 or 0) and vary smoothly across the interfaces. Phase-field modeling is particularly suited for simulating the evolution of the complex SOC microstructures due to its ability to naturally describe topological changes that occur during Ni coarsening, such as merging and splitting of domains [12 - 16].

Similarly to previous work [12-16], four main assumptions are made to simplify the model while capturing the key physical mechanisms:

1. The mass and volume of Ni are assumed to be constant during coarsening since the evaporation of Ni is negligible at typical SOC operating temperatures (500-1000°C) [37].

2. The ceramic phase (YSZ) is considered stationary. This assumption is motivated by previous experimental observations [38, 39] and by the dataset used in the current study [25].

3. The interfacial energy is assumed to be isotropic and constant. Therefore, the effect of crystal orientation on the Ni surface tension is neglected.

4. The contribution of Ni bulk diffusion to the transport of Ni is neglected, and thus, only the contribution of Ni surface diffusion is considered. This assumption is justified by the difference in magnitude between the Ni bulk diffusivity (~10^{-16} m^2/s) and the Ni surface diffusivity ($\sim 1.4\times10^{-11}\, m^2/s$) [40].

An OP, $c(\boldsymbol{x}, t)$, is used to track the Ni phase, where $\boldsymbol{x}$ is the position and t is time. In this work, $c(\boldsymbol{x}, t)$ equals 1 within the Ni phase and 0 elsewhere, and it varies smoothly across the interface between Ni and other phases (YSZ or pore). Its time evolution is described by the conserved Cahn-Hilliard equation:

$$\frac{\partial c}{\partial t} = \nabla \cdot M \nabla \mu, \tag{1}$$

where M is a mobility function and μ is the chemical potential. Following the Ginzburg–Landau formalism [41, 42], the chemical potential μ can be expressed as the functional derivative of the free energy functional F with respect to c [12]:

$$\mu = \frac{\delta F}{\delta c} = \frac{\partial f}{\partial c} - \varepsilon^2 \nabla^2 c, \tag{2}$$

where F is given by $F = \int_V \left[\frac{\varepsilon^2}{2}|\nabla c|^2 + f(c)\right] dV$, ε is the gradient energy coefficient, $f(c) = \frac{Q}{4}c^2(1-c)^2$ is a fourth-order Landau polynomial for the homogeneous free energy of the system, and V is the system volume. In $f(c)$, Q represents the height of the energy barrier between the two minimum energy states, and it sets the energy scale. The gradient energy coefficient ε, together with Q, determines the Ni-YSZ interfacial energy; the two are linked to the interface thickness δ through the relationship $\delta = \varepsilon\sqrt{2/Q}$ [12]. In this work, the interface thickness δ was chosen to be 90 nm, numerically resolved by 5 grid spacings, to limit the error arising from the effect of the diffuse-interface approach while maintaining an adequate numerical resolution and reasonable computational cost.

To account for the presence of stationary YSZ, no-flux boundary conditions (BCs) must be applied at the Ni/YSZ interface, and the equilibrium contact angle prescribed by Young's condition, θ_c, should be imposed at the triple junctions (where the Ni/YSZ, Ni-pore, and YSZ-pore interfaces all meet). The no-flux BCs for Eq. 1 ensure mass conservation, while the contact angle BCs account for the interaction between the Ni and YSZ phases. Using the smooth boundary method (SBM) [43], the YSZ phase is described by a domain parameter, $\psi(\boldsymbol{x})$, which takes the value 0 inside the YSZ (and 1 elsewhere) and varies smoothly across the YSZ interfaces. Note that with this description, the normalized gradient of the domain parameter, $\frac{\nabla\psi}{|\nabla\psi|}$, gives the outward normal vector of the contour level sets of ψ [43] of the YSZ phase boundary. The phase-field equation can then be reformulated as in [43], which reduces to the Cahn-Hilliard equation in the regions where $\psi = 1$, while imposing the BCs in the interfacial region where $0 < \psi < 1$. The contact angle θ_c between Ni and YSZ at the junction can be numerically evaluated in terms of ψ and c according to $(\nabla\psi/|\nabla\psi|) \cdot (\nabla c/|\nabla c|) = -\cos\theta_c$, which must be set to the equilibrium value. Thus, the following equation can be derived [12, 43]:

$$\nabla\psi \cdot \nabla c = -|\nabla\psi| \cos\theta_c \frac{\sqrt{2f}}{\varepsilon}. \quad (3)$$

Following Refs. [12] and [43], by multiplying Eq. 2 by ψ and substituting Eq. 3 into Eq. 2, the Cahn-Hilliard equation that includes no-flux and contact angle BCs is obtained [12, 43]:

$$\begin{cases} \mu = \frac{df}{dc} - \frac{\varepsilon^2}{\psi}\left(\nabla \cdot (\psi \nabla c) + \frac{|\nabla\psi|\sqrt{2f}}{\varepsilon}\cos\theta_c\right) \\ \frac{\partial c}{\partial t} = \mathrm{M}\left[\frac{\nabla\psi}{\psi} \cdot \nabla\mu + \nabla^2\mu\right] \end{cases} \quad (4)$$

Note that a small number (10^{-6}) is added to ψ to avoid division by zero in the calculation of the right-hand side of the equations. Finally, we employ the mobility function proposed by Davis et al. [16] for the surface mobility M, expressed by

$$M = M_0\left\{a_1\left[1 - \tanh\left(\frac{|\nabla\psi|^2}{\omega}\right)\right]\tanh\left(\frac{|\nabla c|^2}{\omega}\right) + a_2\tanh\left(\frac{|\nabla\psi|^2}{\omega}\right)\tanh\left(\frac{|\nabla c|^2}{\omega}\right) + a_3\left[1 - \tanh\left(\frac{|\nabla c|^2}{\omega}\right)\right]\tanh\left(\frac{|\nabla\psi|^2}{\omega}\right)\right\} \quad (5)$$

where M_0 is the mobility prefactor. The first term inside the curly brackets on the right-hand side of Eq. 5 accounts for the mobility at the Ni-pore interface, the second term accounts for the mobility of Ni on Ni-YSZ interface, and the last term accounts for the mobility of Ni at the YSZ-pore interface. The prefactors a_1, a_2, and a_3 control the weight of each term [16]. As a note, a polynomial form of a mobility function was also considered. We found that the better agreement between the simulation and experiment was obtained using Eq. 5. The simulation time required for the implementation of Eq. 5 is approximately double as compared to when using the polynomial mobility function; however, the extra computational expense was acceptable, given the better match with the experimental results.

3.2 Numerical implementation

The following dimensionless parameters are introduced in Eq. 6 to obtain dimensionless equations [16]:

$$\bar{L} = \frac{L}{L_0}, \quad \bar{t} = \frac{t}{\tau}, \quad \bar{\varepsilon}^2 = \frac{Q}{2E}, \quad \bar{Q} = \frac{QL_0^2}{E\delta_s^2}, \bar{M}_0 = \frac{M_0 E \tau}{L_0^2}, \tag{6}$$

where L_0 and τ are the characteristic length (chosen to be equal to the voxel size of 18 nm) and the characteristic time, respectively, and E is a reference energy density [16]. The mobility prefactor M_0 can be expressed as a function of the diffusion coefficient as $M_0 = D_s\left(\frac{\partial^2 f}{\partial c^2}\right)^{-1}$. Using the dimensionless parameters in Eq. 6, an estimation of the characteristic time is given by:

$$\tau \sim \frac{L_0^4\left(\partial^2 f/\partial c^2\right)_{C_{eq}}}{ED_s\delta_s^2} \simeq \frac{\bar{\varepsilon}^2 L_0^4}{D_s\delta_s^2}, \tag{7}$$

where D_s is the surface diffusion coefficient of Ni on Ni surface, experimentally measured to be in the range of 8×10^{-12} to $1.4\times10^{-11}\, m^2/s$ at 800°C, depending on the impurity concentration [40]. In this work, we take the average between these values to set $D_s = 1.1\times10^{-11}\, m^2/s$. The physical interface thickness δ_s, used for computing the characteristic time (Eq. 7), is assumed to be equal to the lattice constant of Ni, which equals to $3.5\times10^{-10}\, m$ [40]. The characteristic time obtained for this parameter set is approximately $8.56\times10^{-4}\, s$. The prefactors a_1, a_2, and a_3 are set to 1.0, 0.1, and 0.1, respectively, in accordance with the values used by Davis et al. [16], who assumed metallic surface diffusion to be the dominant mechanism for Ni transport. This choice sets the Ni surface diffusion (on Ni-pore interface) to be the primary transport mechanism, while leaving Ni transport via Ni-YSZ interface and pore-YSZ surface to have marginal roles in the microstructure evolution. The parameters used for the simulations and for the computation of the characteristic time are summarized in Table 1.

Table 1: Parameters used for the simulations and experimental values used for the calculation of the characteristic time.

δ	L_0	$\bar{M}_0$	$\bar{\varepsilon}$	$\bar{Q}$	ω	a_1	a_2	a_3	D_s	δ_s
90 nm (5 grid spacings)	18 nm	1.0	0.1	0.02	0.1	1.0	0.1	0.1	1.1×10^{-11} m^2/s	3.5×10^{-10} m

Spatial discretization was performed with the central difference method, and time discretization was performed with the explicit forward-Euler scheme. The grid spacing was chosen to be $\Delta x = \Delta y = \Delta z = 1.0L_0$, while we set $\Delta t = 1.25\tau$. The von Neumann analysis [44] of the linearized version of Eq. 4 was used to define the time step to ensure numerical stability given by $\Delta t \leq \frac{\Delta x^4}{72\, M\bar{\varepsilon}^2}$; the time step obtained with this relation did not cause any numerical instabilities. Neumann BCs were applied at the boundaries of the computational domain for both μ and c to set zero flux at these boundaries. These BCs ensure that the mass within the volume remains constant within the numerical accuracy throughout the simulation.

The initial condition for the simulations was set by a subvolume of the 3D reconstruction obtained for the cell before annealing. The size of the subvolume selected for the simulations is 301 × 301 × 301 voxels, corresponding to approximately 5.4 × 5.4 × 5.4 μm^3. The initialization of the order parameter and domain parameter was performed as described by Yu et al. [43]; the sharp interfaces between the three phases in the segmented volumes were smoothed for both the evolving order parameter c and the stationary domain parameter ψ in this step. This step involved generating a corresponding signed distance function and evaluating its hyperbolic tangent function [43]. Only the order parameter for the Ni phase was allowed to evolve during the simulation, while the domain parameter for the YSZ was fixed.

For comparison with the experimental microstructure, each simulated volume was segmented using the order parameter c and the domain parameter ψ as follows:

$$\begin{cases} c > 0.5 \ \cap \ \psi > 0.5 & \text{Ni phase} \\ \psi < 0.5 & \text{YSZ phase.} \\ c < 0.5 \ \cap \ \psi > 0.5 & \text{Pore phase} \end{cases} \quad (8)$$

Microstructural characteristics, such as the specific surface and interfacial area per unit volume, TPB density, and phase connectivity, were computed every 10^5 iterations on the segmented volumes. The Ni PSD was evaluated every 10^6 iterations.

The simulation code was written in C++ and was parallelized using the Message Passing Interface (MPI) protocol to expedite the run time. The 3D domains for the different simulations performed in this work were decomposed into nearly cubic subdomains, which were distributed among the processors.

3.3 Contact angle validation

To validate the simulation code with the selected parameter set, a droplet placed on a surface of another material was simulated to ensure that the contact angle and no-flux BCs were accurately imposed. The simulated volume sizes were $L_x = L_y = L_z = 100$, with $\Delta x = \Delta y = \Delta z = 1$. A flat horizontal domain interface was defined via a hyperbolic tangent function such that $\psi = 0.5$ at $z = 30$. The domain parameter ψ range was 10^{-6} to 0.5 for $z < 30$ (the small value avoids division by zero) and 0.5 to 1 for $z > 30$, varying smoothly in the interfacial region. The computational domain was initialized with a cube having an edge length of 30 grid points and was centered at x = 50, y = 50, and z = 45. The order parameter was set to 1 inside it and 0 outside.

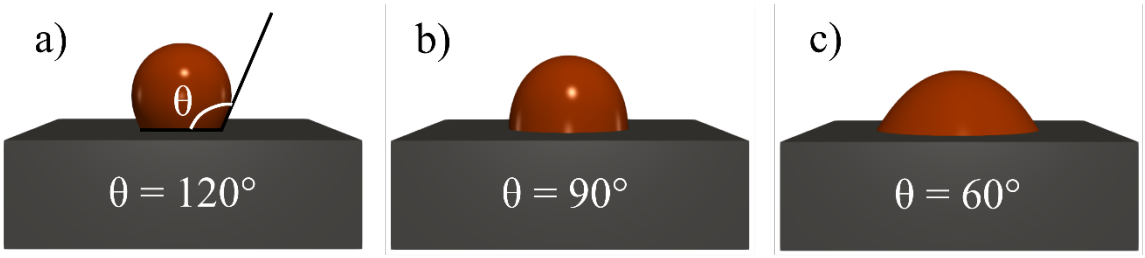

Figure 1. Simulation of a droplet on a flat surface with different equilibrium contact angles. The contact angle value set in the simulation (θ) is also reported in the picture for the three simulations performed: (a) θ_c=120°, (b) θ_c=90°, and (c) θ_c=60°.

The system was simulated with the mobility function in Eq. 5 using $\bar{M}_0 = 1$, $\bar{\varepsilon} = 0.1$ and $\bar{Q} = 0.02$. Simulations were run with three equilibrium contact angles, θ_c= 60° (Figure 1a), 90° (Figure 1b), and 120° (Figure 1c) to observe mostly wetting, neutral, and mostly non-wetting behavior, respectively. The cosine of the contact angle, $\cos\theta$, from the simulation was estimated by obtaining the average of $-\frac{\nabla\psi\cdot\nabla c}{|\nabla\psi||\nabla c|}$ in the region where both $0.1 < \psi < 0.9$ and $0.1 < c < 0.9$ [43]. The error between the angle reached at equilibrium and the angle imposed as a BC was computed as $\frac{\cos\theta - \cos\theta_c}{2}$, where the factor 2 takes into account the total variation in the cosine function magnitude [43].

In the SBM, errors in the equilibrium contact angle may arise from the diffuse nature of interfaces. To reduce this error, the width of the interfaces (represented by the domain parameter and OPs) should be chosen to be sufficiently small compared to the natural length scales of the system (e.g., the radius of curvature), which in turn must be resolved by the discretized grid to ensure sufficient numerical accuracy [43]. The results show that the maximum error was obtained for an imposed angle of 120°, and the error in the cosine was less than 3 %, corresponding to a maximum angle variation of 5°. The complexity of the real Ni/YSZ microstructure makes the computation of the contact angle challenging, increasing the uncertainty in the quantification. Therefore, the error analysis on the

279 contact angle was performed only for the simplified droplet structure illustrated in Figure 1. Higher
280 accuracy can be achieved by decreasing the thickness of the diffuse interface δ, but this decrease will
281 lead to a significantly larger computational cost; the selected parameter set provides a suitable
282 compromise between accuracy and computational efficiency.

283 Furthermore, the accuracy of the no-flux BCs imposed at the interior boundaries ($\nabla\psi \neq 0$) was
284 examined by numerically computing the volume integral of c, which reflects the total volume of the
285 droplet in the system. In particular, the volume ratio, $\frac{\int \psi c(t_e) d\Omega}{\int \psi c(t_0) d\Omega}$, where t_e is the time required to reach
286 near equilibrium state and t_0 is the initial time of the simulation, was computed over the region where
287 $\psi > 0.5$ [43], which should remain unity when the volume is constant. In all validation simulations,
288 the error was within 1 %, indicating that the no-flux BC imposed by the SBM sufficiently ensures
289 mass conservation in the simulation.

290 **4. Results**

291 *4.1 Nickel particle size and specific surface and interfacial areas*

292 Figure 2 shows the simulated time evolution of the Ni mean particle radius for different θ_c. The
293 equilibrium contact angles of θ_c= 97°, 120°, and 150° between Ni and YSZ were examined to observe
294 their impact on the morphological evolution. Although the exact equilibrium contact angle between
295 Ni and YSZ is unknown, dewetting behavior of Ni on YSZ was experimentally observed [45] and
296 thus wetting and mostly wetting equilibrium contact angles (less than 90°) were not considered in
297 this study. The contact angle was calculated on both the pristine and annealed experimental samples
298 using the method described in Sec. 2.2. The resulting contact angle was 83° for the pristine
299 microstructure and 103° for the treated microstructure.

300 Trends of increasing particle radius observed in all simulations are similar to the experimental
301 observation by Faes et al. [11] and Tanasini et al. [39]. Although the Ni mean radius increases for all

the θ_c, the mean radius increases with increasing θ_c, i.e., as the Ni becomes more non-wetting. In the experimental data, the mean particle radius increases from 300 nm in the pristine cell to 384 nm after three hours of annealing, as shown by the black dashed line in Figure 2. The experimental value of the Ni mean radius was reached after ~4.3 hours for θ_c=150°, while for θ_c=120° and θ_c=97°, the Ni mean radius was below the experimental value throughout the entire simulation. It is interesting that the coarsening becomes extremely slow for θ_c=97°, which may indicate that, if the equilibrium contact angle could be reduced (for example, by introduction of additional chemistry), it may be possible to nearly stabilize the Ni/YSZ microstructure.

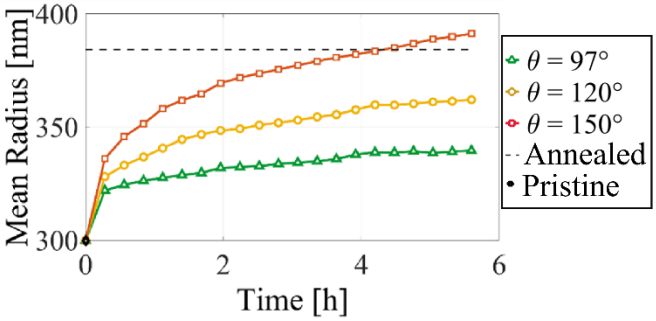

Figure 2: Average Ni particle radius calculated every 10^6 iterations (~18 minutes of physical time) for each simulation. The horizontal dashed line represents the Ni mean radius computed for the experimental volume annealed for three hours, indicated by the star.

The time evolutions of the specific Ni surface area and the specific Ni/YSZ interfacial area are shown in Figures 3a and 3b, respectively. Trends of decreasing specific Ni surface area are observed for all three equilibrium contact angles simulated. For the overall Ni surface area, the experimental value of ~1.4 $\mu m^2/\mu m^3$ (observed after three hours of annealing) is reached for θ_c=120° and θ_c=150° after ~5 and ~1.5 hours, respectively. However, the results with θ_c=97° overestimate the experimental value over the entire period simulated. The simulated specific Ni/YSZ interfacial area reached the experimental value (0.79 $\mu m^2/\mu m^3$) after ~2.1 hours for θ_c=120° and after ~0.1 hour for θ_c=150°.

322 Finally, for the case of θ_c=97°, the specific Ni/YSZ interfacial area decreases only slightly, remaining
323 greater than the experimental value for the entire span of the simulation.

324 *4.2 TPB and phase connectivity*

325 Figures 3c and 3d show the time evolutions of the total and percolating TPB densities, respectively.
326 For θ_c=97° and θ_c=120°, the results show a pronounced decrease in the total TPB density during the
327 first two hours, reaching the experimental value of 2.54 μm/μm^3 after ~1 hour in both cases.
328 Interestingly, the simulation run with θ_c=150° results in the least decrease in the TPB density,
329 reaching the experimental value after ~4.5 hours. The percolating TPB density, Figure 3d, shows a
330 pronounced increase surpassing the experimental value in the first ~18 minutes for all of the
331 equilibrium contact angles. After this initial increase, the percolating TPB density starts decreasing,
332 and the experimental value (2.13 μm/μm^3) is reached between 1.1 and 1.7 hours in all cases.

333 Figure 3e shows the time evolution of the pore network connectivity. In the early stages of the
334 simulations, the connectivity of pores suddenly increases from ~70 % to ~95 - 99 % for all three
335 simulated cases. After 5.6 hours, the results show an increase in pore connectivity (with values in the
336 range 97-99 %, for the three values of θ_c simulated), reproducing the experimental value of ~98 %,
337 as shown in Figure 3e. The Ni connectivity evolution results (not illustrated in Figure 3) show only
338 small fluctuations around the initial value of ~97.8 % for all simulations. The connected Ni fraction

after three hours of annealing was computed to be 97.4 % in the experimental data, while the values obtained at the end of all simulations were in the range of 97.3-97.9 % for all the θ_c simulated.

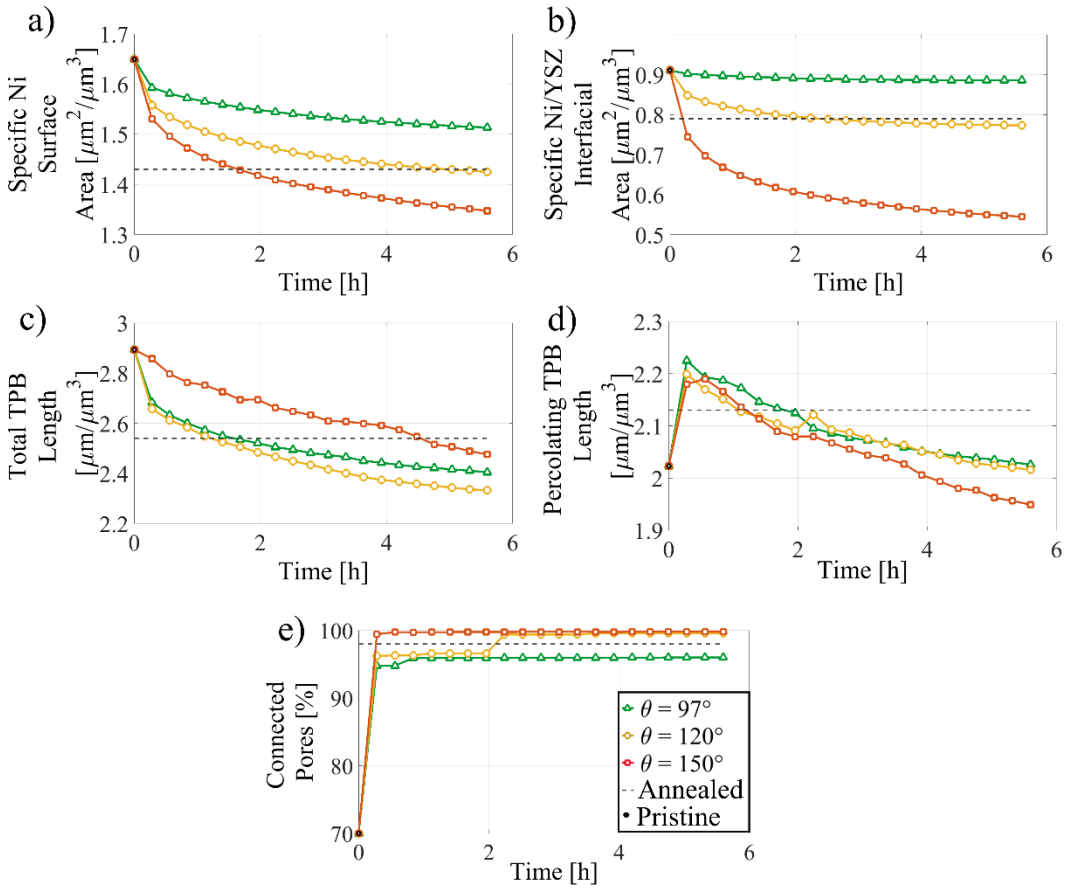

Figure 3: Time evolutions of (a) the specific Ni surface area, (b) specific Ni/YSZ interfacial area, (c) total TPB density, (d) percolating TPB density, and (e) pore connectivity for all equilibrium contact angles θ_c considered. The experimental values for pristine and annealed samples are indicated by the circle at time of 0 and a dashed line, respectively.

4.3 Local morphological changes in the Ni/YSZ microstructure

Figures 4a and 4b illustrate selected slices extracted from the pristine and annealed microstructures from experiments, while Figures 4c - 4e show the same cross-sections obtained from the simulated datasets for different θ_c.

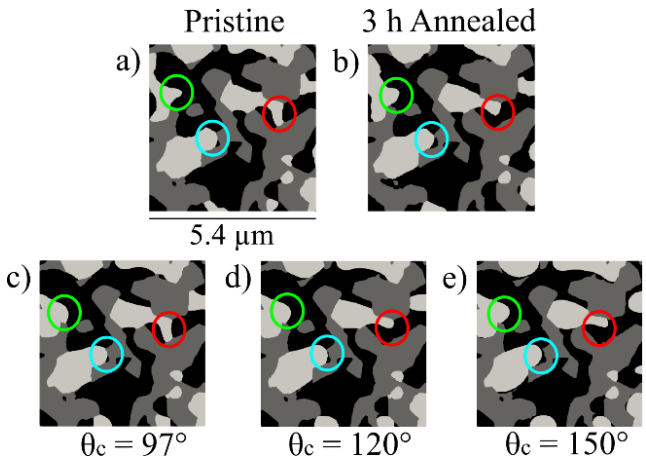

Figure 4: Representative two-dimensional slices of the segmented three-dimensional volume for the cell (a) in the pristine state and (b) after three hours of annealing, along with the corresponding simulation results of three-hour coarsening for the three θ_c employed: (c) 97°, (d) 120°, and (e) 150°. The light gray is Ni, the darker gray is YSZ, and black is the pore region. Decreases in curvature during coarsening (green circle) and Ni dewetting from the YSZ scaffold (red and blue circles) are illustrated.

From visual inspection, a reduction in surface curvatures of the Ni phase (light gray) is observed across the cermet for both the annealed structure and the simulated structure (additional examples can be found in the supplementary materials). As an example, sharp features of the Ni network, highlighted by the green circle, evolve towards more rounded shapes in both the experimental structure and all simulations. However, a more pronounced curvature reduction is observed in the simulated data, with greater effect seen with increasing θ_c.

Figures 4a and 4b show that some features, characterized by well-defined facets (i.e., visually flat surfaces) in the pristine state, preserve their shape in the three-hour annealed structure in experiments. For instance, focusing on the blue circles, only minor morphological changes are observed in the experimental data. On the other hand, the simulation results show the evolution of the well-defined

366 facets to an almost rounded shape. The same trend can be observed for the features in the green and
367 red circles. This discrepancy may be either due to the surface energy anisotropy that is not taken into
368 account in the simulation or due to the mobility of the interface, which may be overestimated in the
369 simulation.

370 The red circles in Figure 4 highlight an example of Ni dewetting. At this location, the experimental
371 data show that Ni, attached to the YSZ (dark gray) in the pristine microstructure (Figure 4a), detaches
372 after three hours of annealing (Figure 4b). In the simulated structures, this phenomenon is not
373 observed for θ_c=97° while both simulations with θ_c=120° and θ_c=150° (Figures 4d and 4e) show Ni
374 dewetting (more instances are provided in the supplementary materials).

375 After three hours, the simulation with θ_c=97° leads to the least pronounced microstructural changes,
376 while a more pronounced Ni dewetting and curvature reduction compared to the experimental data
377 are observed for θ_c=150°. Finally, based on visual inspection, the best agreement between the
378 experiment and simulations is obtained for θ_c=120°.

379 *4.4 Nickel network interface shape distribution*

380 Calculating the local curvature for the Ni network and plotting the probability distribution of the
381 principal curvatures (κ_1 and κ_2) in the form of ISD gives an indication of the morphology of the
382 features present in the volume.

383 Figure 5 shows ISD plots for the pristine and annealed microstructures, as well as simulated
384 microstructures at the simulation time equivalent to three hours of annealing. The probability
385 distribution of the surface curvature for the pristine microstructure (Figure 5a) appears to contain two
386 populations of Ni surfaces, one with an even distribution of concave and convex surface features
387 (with almost symmetrical distribution around the line where κ_1 = - κ_2 (zero mean curvature line)),
388 and the other having cylindrical shapes (along κ_1 = 0). After three hours of annealing, the ISD peak

shows a shift from quadrant II towards quadrant I, indicating an increase in convex features after coarsening.

Figure 5c (θ_c=97°) shows a high probability for features characterized by $\kappa_2 \sim 0$ and $\kappa_1 < 0$, corresponding to a tube-like shape of the Ni phase, as shown by the red region highlighted by the purple arrow in Figure 5c. This result indicates the presence of many concave features in the Ni network where Ni wets convex YSZ areas. The rest of the features have curvature values almost equally distributed around the zero mean curvature line, reminiscent of the pristine dataset.

Figure 5d shows the ISD plot for θ_c=120°, with the high-intensity region located around $\kappa_2 = -\kappa_1$, which is less intense than the peak at $\kappa_2 \sim 0$ in the θ_c = 97° result. The probability distribution of the interface shapes in Figure 5d shifts towards quadrant I, indicating that the number of concave features decreases while the number of convex features increases. The shift towards more convex shapes is even more pronounced for θ_c=150° (Figure 5e), where we observe a region of high intensity in quadrant I and very small population where $\kappa_2 < 0$, which corresponds to concave Ni shapes.

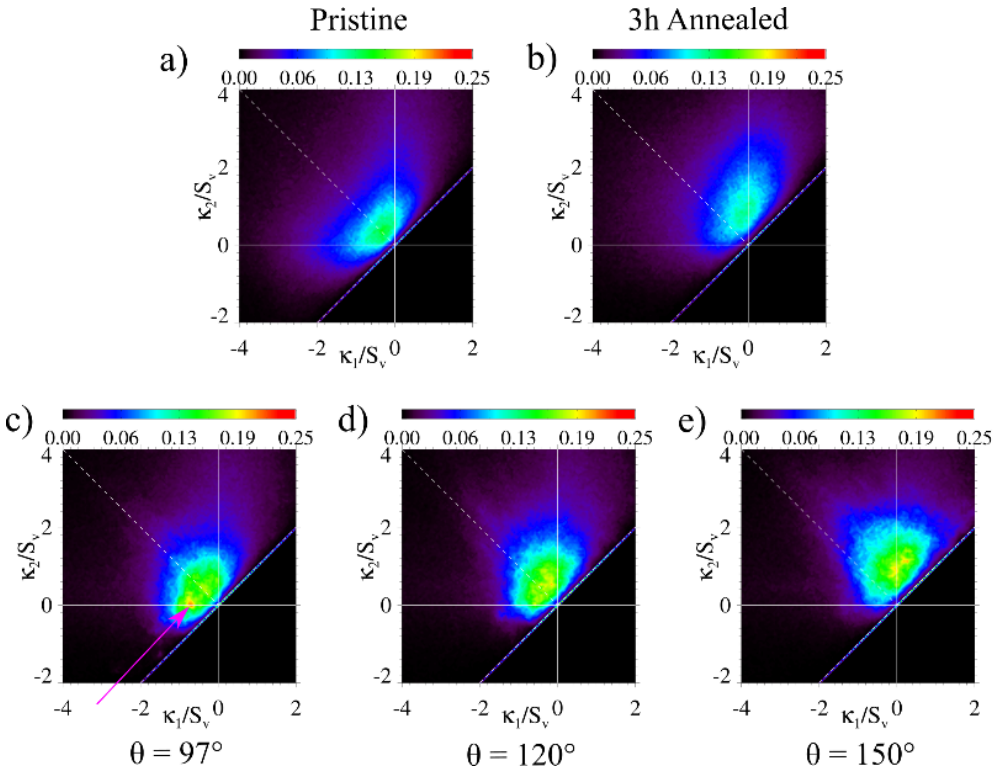

Figure 5: ISD plots of the Ni phase for the experimental data of (a) the pristine state and (b) after three hours of annealing, together with the ISD plots for the three-hour annealed simulated microstructure with different θ_c: (c) 97°, (d) 120° (d), and (e) 150°.

5. Discussions

5.1 Physical interpretation of the evolution of the statistical characteristics of the microstructure

The Ni coarsening process is driven by curvature reduction and the accompanying interfacial area reduction [5, 9, 10, 12, 16]; this phenomenon promotes the formation of smoother and larger Ni particles, resulting in an increase in the Ni mean particle radius, as observed in Figure 2. This particular trend was previously reported in several experimental studies [9-11, 39, 46], where different cells were analyzed after tests. Vaßen et al. [9] found a mathematical correlation for Ni particles growth in a Ni/YSZ electrode annealed at 1000°C for 4000 hours. Faes et al. [11] computed the size of Ni particles in cells tested as part of different stacks in the rage of 700-800°C from approximately 150 to more than 1000 hours. The cells tested from Tanasini et al. [39] were operated

at 850°C and the particles size was computed at the beginning of the test and after 24, 200, and 1000 hours. Chen-Wiegart et al. found the same trend for Ni particles size when examining Ni coarsening via ex-situ X-ray nanotomography [46] in the first 92 hours of the cell aged at 1050°C. The trends are also in agreement with other modeling works, such as that of Davis et al. [16], which was initialized with artificially constructed geometries. Despite the difference in the structure, the qualitative agreement is perhaps not surprising since the excess interfacial energy, which is proportional to the interfacial area, drives the evolution.

Figure 2 shows a more pronounced increase in the Ni mean radius as θ_c increases. This increase is explained by the enhanced tendency of Ni particles to dewet and coarsen with increasing contact angles, instead of wetting the YSZ [12, 16, 47]. The large equilibrium contact angle drives the system to evolve to reduce the Ni/YSZ interface. Indeed, Figure 3b shows lower specific Ni/YSZ interfacial areas with increasing θ_c. This is in agreement with the results reported by Kennouche et al. [48] obtained via postmortem X-ray tomography.

In comparison to these findings, the overall TPB density (Figure 3c) shows somewhat unintuitive results. Specifically, the overall TPB density for the θ_c=150° case decreases more slowly compared to the simulations with θ_c=97° and θ_c=120°. A similar trend was observed by Davis et al. [16] in Ni coarsening simulations starting from artificially constructed structures. They suggested that, with low wettability, the Ni network can form closed TPB loops, thus increasing the total TPB density.

Finally, based on the ISD in Figure 5, it is evident that the probability of finding convex elliptic surfaces increases as the contact angle increases. The high prevalence of concave Ni features for θ_c=97°, as shown in Figure 5c, results from the tendency of Ni to wet convex YSZ features, thus increasing the integrated probability lying in quadrant II of the ISD plots. When the wettability decreases (i.e., the equilibrium contact angle increases), this effect is hindered, and therefore more

convex features develop in the microstructure. Similar results were obtained for the artificially constructed Ni/YSZ geometries studied by Davis et al. [16].

Generally, the least amount of microstructure evolution is observed for θ_c=97°, suggesting that one possible strategy for limiting Ni coarsening is to increase the Ni/YSZ wettability, as also suggested in [12, 16, 49]. Furthermore, the simulation results for θ_c=120° gives the best overall match with the experimental results. This value is in line with contact-angle measurements performed by Tsoga et al. [45], in which a minimum contact angle of ~117° was found for Ni on YSZ at 1500°C. Mantzouris et al. [50] suggest that the linear relationship between interfacial energies holds approximately for both a liquid and solid metal on ceramic. Assuming this, the contact angle between Ni and YSZ at 850°C can be expected to be in the same range as the one measured by Tsoga et al. at 1500 °C.

Additionally, Table 2 shows the contact angle values computed on the simulated geometries at different time steps. It can be observed that after three hours the simulations with θ_c=120° and θ_c=150° have not reached the equilibrium contact angle set and are still evolving. We can notice that, in the case of θ_c=120°, for the majority of the simulation time, the contact angle assumes values between 105-109°. Among the cases examined in this work, these values are the closest to the one measured in the experimental data (θ_c=120°), likely explaining the best match observed for the imposed θ_c=120°.

Table 2: Contact angle values computed on the simulated geometries at different time steps

Time	Contact angle values for the simulation with θ_c=97°	Contact angle values for the simulation with θ_c=120°	Contact angle values for the simulation with θ_c=150°
18 minutes	95°	105°	124°
36 minutes	95°	106°	128°

54 minutes	95°	107°	130°
1.2 hours	95°	107°	131°
2.4 hours	96°	109°	134°
3 hours	96°	111°	135°

457

458 *5.2 Direct comparison between experimental and simulation results*

459 Figure 6 shows a comparison between subvolumes of the experimentally reconstructed Ni networks
460 and the corresponding simulation results taken at the simulation time equivalent to three hours of
461 coarsening. Figure 6b shows how the feature highlighted by the blue arrow evolves from a concave
462 shape in the pristine state towards a more convex shape after three hours of treatment. Magnifications
463 of the regions highlighted by the blue arrows are also included in Figure 6a and Figure 6b to better
464 show the Ni surface morphology. The simulation with θ_c=97° (Figure 6c) shows that the concave
465 shape is mostly preserved. While we present only one example here, the same phenomenon is
466 observed throughout the entire Ni network, as shown by the ISD plot in Figure 5c. In fact, the ISD
467 diagram for θ_c=97° presents a peak in the probability distribution in quadrant III, meaning that the
468 structure contains many concave shapes. For θ_c=120° (Figure 6d), the evolution of the feature
469 highlighted by the blue arrow towards a more convex shape is observed; this effect is more
470 pronounced for θ_c=150° (Figure 6e). This observation is in line with the ISD diagrams in Figures 5d
471 and 5e, where the local curvature probability distribution shifts towards quadrant I, indicating the
472 presence of more convex shapes.

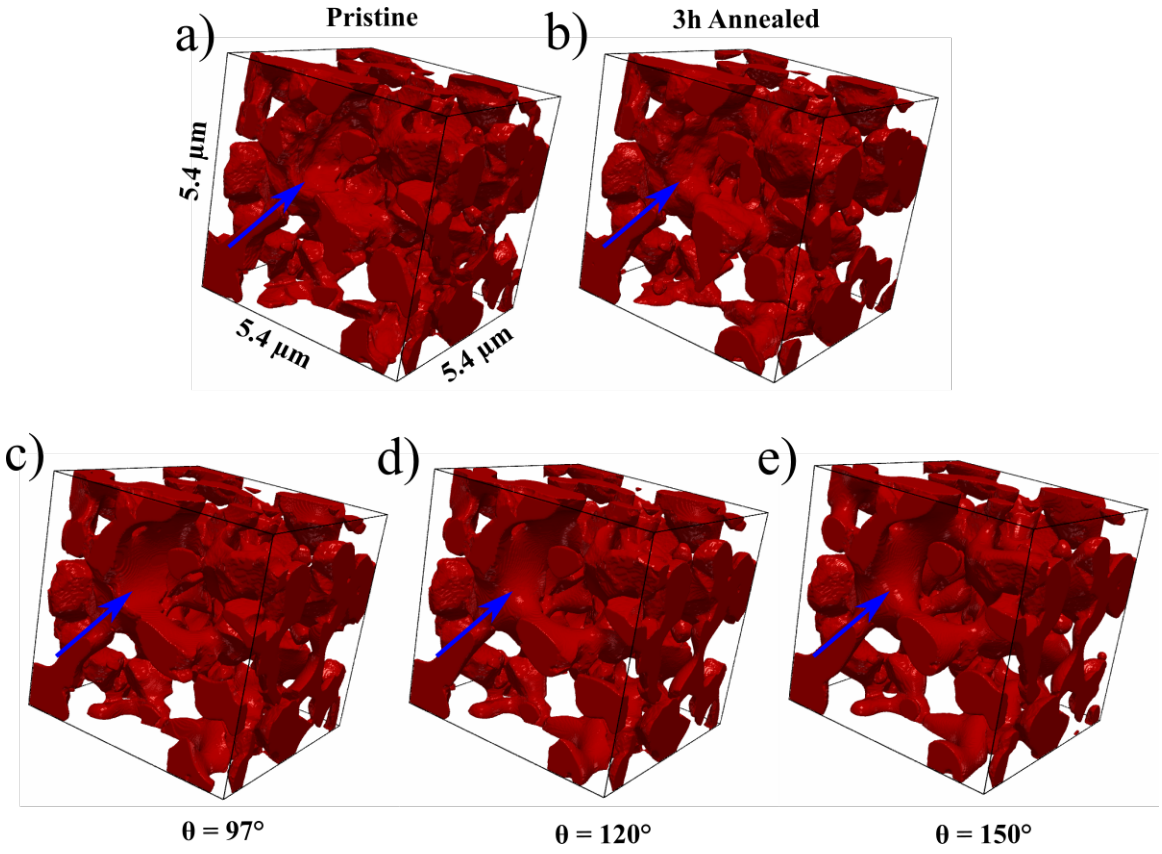

Figure 6: Three-dimensional renderings of the Ni phase for the (a) pristine and (b) three-hour annealed states and the simulation results for θ_c= (a) 97°, (b) 120°, and (c) 150° at the simulation time (t=3 hours).

The blue arrow in Figure 6a and 6b points to an example location in the experimental data where the preservation of flat Ni surfaces during coarsening can be observed. In Figure 6b, the blue arrow also hints at the presence of grain boundaries, which also seems to be preserved during coarsening. In contrast, in all simulations, the flat surfaces in the pristine microstructure disappear in favor of more rounded and smoother surfaces.

The phase-field model employed here does not account for anisotropy in the interfacial energy and mobility, and it also ignores the polycrystalline nature of the Ni network. However, there has been evidence that the anisotropy in Ni surface energy [15] and surface diffusion coefficient [12], as well as the presence of grain boundaries, do have an effect on the morphological evolution of Ni during coarsening [13, 14, 15, 17]. The comparison of our simulation and experimental results indicates that these effects may be indeed significant under typical SOCs operating conditions.

In phase-field modeling, multiple OPs, each of which tracks one or more grains in a polycrystalline structure, can be used to include crystallographic information [14, 15]. Such a phase-field model is expected to produce results that better match the experimental data. Interfacial anisotropy can also be incorporated [15]. However, obtaining 3D microstructures that contain the crystallographic information needed for the validation of a phase-field model for polycrystalline materials, is an open challenge and cannot be achieved by tomographic techniques such as FIB-SEM or standard X-ray tomography. 3D X-ray diffraction (3D-XRD) offers the potential to obtain 3D structures containing crystallographic information [51] but currently lacks the spatial resolution needed for typical Ni/YSZ electrodes.

5.3 Pore connectivity

The SOC performance is strongly influenced by the pore connectivity, as it is necessary for the pore network to provide the transport paths to TPBs in order to keep them electrochemically active. In our previous work [25], a significant increase in pore connectivity after three hours of annealing was observed. Figure 3e shows that the evolution of the pore connectivity, mainly at the beginning of each simulation, is not strongly affected by the imposed θ_c. Therefore, only the results for θ_c=120° are presented, which generally provides best match to the experiment (see above) and also supported by the experimental measurement by Tsoga et al. [45].

Figure 7 shows the 3D evolution of the pore connectivity for the system simulated with θ_c=120°. In this analysis, which follows the approach in Ref. [52], any region of the pore network not in contact with any of the faces of the analyzed volume is considered “disconnected” (0-side contact). In contrast, a “connected” (6-side contact) region is connected to all the faces, and “unknown” (from 1- to 5-side contact) connectivity is assigned to regions in contact with only one or some of the faces. To facilitate the analysis, only regions characterized by unknown connectivity (yellow) and

disconnected pores (red) are presented for both the experimental data (Figures 7a and 7b) and simulation results (Figures 7c-7e).

The experimental results in Figures 7a and 7b show a significant increase in pore connectivity after three hours of annealing, indicated by the decrease in pores with "unknown" connectivity, without changes in the isolated porosity. Figure 3e shows that in the first 1.5 min of the simulation, the pore connectivity rapidly increases from ~70 % to ~95 % for θ_c=120°. In this study, a stepwise increase in pore connectivity is observed as large chunks of the pore network become connected in discrete events. However, the three-hour coarsening simulation (Figure 7f) shows a small underestimation of pores with unknown connectivity, while almost no change in isolated pores is in line with the experimental results (Figure 7b).

Figures 7c-7e show the pore connectivity in the early stages of the annealing process between 0 and ~1.5 min. The three time steps shown represent the instants where a variation in the connectivity was detected: 10 s (Figure 7c), 14 s (Figure 7d), and 88 s (Figure 7e). The connectivity after a simulated time of three hours is shown in Figure 7f. Linking the early connection of pores (Figures 7c-7e) with the fast early disappearance of features characterized by high curvature that cannot be resolved due to the thickness of the smooth interface is not trivial (discussed further in Section 5.4). However, since the pore connection occurs after the interface is relaxed, the simulation results are likely not artifacts due to the relaxation of the interface. Moreover, the early evolution of the pore connectivity is highly sensitive to small variations in the Ni network. In fact, small changes in the Ni morphology, causing Ni dewetting or domain splitting, can suddenly open new pathways, connecting previously disconnected pore regions. Further in situ tomographic studies with high time resolution is needed to provide further insights into the mechanism of pore connectivity evolution.

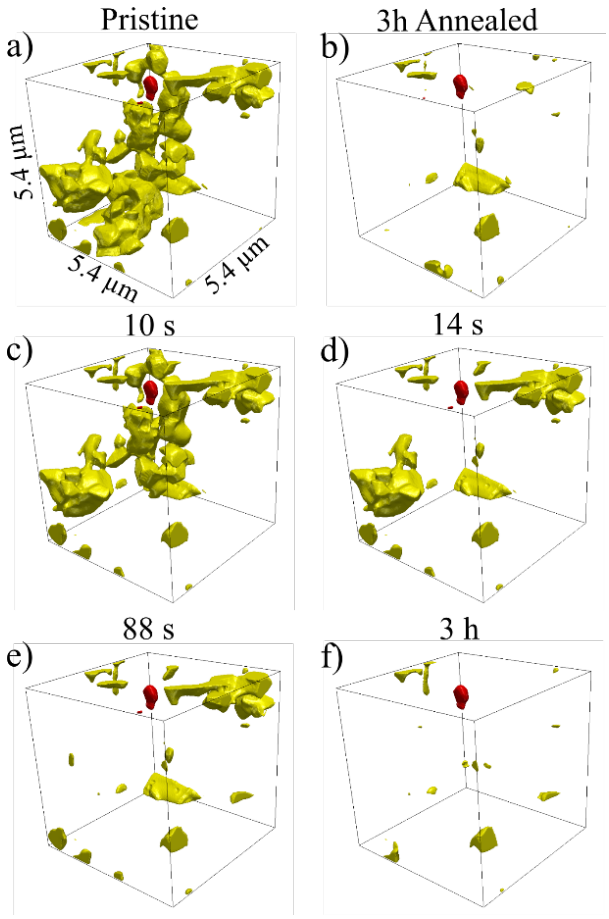

Figure 7: Three-dimensional renderings of the unknown and disconnected porosity for the (a) pristine and (b) three-hour annealed microstructures, along with simulation results with θ_c=120° after (c) 10 s, (d) 14 s, (e) 88 s, and (f) three hours. Unknown porosity is shown in yellow, and isolated porosity is shown in red.

5.4 Sources of errors

Several sources of errors affect the quantitative accuracy of the simulation predictions and must be discussed. First, we employ a diffuse interface approach, wherein a diffuse interface with a finite thickness is used to represent an interface between two phases. Consequently, features comparable or smaller than the interface thickness cannot be represented [35, 49] and also affects the accuracy of the simulated evolution of small features. While the model is expected to be accurate when the feature sizes are sufficiently larger than the width of the diffuse interface (90 nm in this work), the evolution of small particles (comparable to a few times this thickness) could be significantly overestimated.

544 Nevertheless, such small particles tend to be absorbed into nearby larger particles quickly and
545 therefore are expected to have little influence on the overall evolution.

546 Uncertainties in important experimental parameters, such as the surface diffusion coefficient,
547 interfacial energy, and physical interface width, leads to a compounded uncertainty in the
548 characteristic time of the simulations, making comparisons with experimental data challenging.
549 Moreover, the mobility function implemented and the θ_c value set in the model has a strong impact
550 on the morphological evolution of the Ni coarsening; thus, we selected a mobility function yielded
551 results that matched the experimental results best. The accuracy of image segmentation is important
552 in comparing experimental and simulation results; in particular, the segmentation error of the pristine
553 microstructure can influence the simulated evolution of the microstructure, especially for pore
554 connectivity, which is highly sensitive to the initial microstructure as discussed above. In addition,
555 segmentation error close to TPBs results in incorrect Ni/YSZ contact angles, which may affect the
556 subsequent evolution.

557 The prefactors a_1, a_2, and a_3 that set the relative values of surface/interfacial diffusivities are set such
558 that accounting for the higher surface diffusion coefficient at the Ni/pore interface compared to the
559 coefficient at the Ni/YSZ and YSZ/pore interfaces. The simulation results may depend on the choice
560 of the prefactors; for example, if Ni surface diffusion on YSZ surface is important, the additional Ni
561 transport paths would accelerate the coarsening process. Such an investigation is out of the scope of
562 this paper and additional studies, as well as experimental determinations of relevant diffusivities,
563 would be needed to increase the accuracy of the model.

564 Finally, to achieve a precise comparison between experiments and simulations, the model
565 assumptions and BCs should be consistent with the experimental ones. Particularly, for what concern
566 BCs it is worth mentioning that the use of experimentally determined microstructures for the
567 simulation prevents to set fully consistent boundary conditions regardless of the choice of the

boundary conditions. In particularly, the choice of periodic BCs show two main problems: a) discontinuity in order parameter values when the same-sized domain is used, and b) discontinuity in the gradients of the order parameter values when the domain is mirrored to make the order parameter values to be continuous. The former is problematic, and the latter is computationally expensive. For what concerns the ex-situ experiments, such as the one presented here, it must be considered that it might not be optimal since the sample is heated and cooled between different scans, which could induce microstructural changes due to the thermal history not considered in the model. Therefore, for a more precise comparison, in-situ experiments performed under a constant temperature are desirable.

6. Conclusions

The first validation of a three-dimensional phase-field model for Ni coarsening in a typical Ni/YSZ electrode was presented, comparing simulation results with time-dependent ex-situ tomography data. A pristine geometry was used as input for the phase-field simulations, and its evolution was discussed in comparison with the same structure experimentally reconstructed after three hours of annealing in H_2 at 850°C.

A phase-field model with a surface mobility function and the smoothed boundary method was employed. Three different equilibrium Ni/YSZ contact angles were simulated, and the effect of this parameter on the Ni coarsening was discussed. Microstructural characteristics, such as the mean Ni radius, specific surface area, TPB density, and interface shape distribution, were computed for both the experimental microstructures and simulation results. In both the direct comparison between the experimental and simulated 3D structures and the interface shape distribution, it was observed that initially concave surfaces of Ni phase become more convex. The analysis of the pore network connectivity reveals that the model can reproduce the final improved connection between pore regions, in line with experimental observations. These simulation results agree qualitatively with

previous experimental observations and modeling results. Furthermore, the equilibrium contact angle of 120º provided the overall best match to the experimental data. The discrepancy between simulation and experimental results is likely due to effects that are not considered in the model, including surface energy anisotropy, as well as due to the uncertainties in input parameters. In particular, the assumptions of isotropic interfacial energy and surface diffusion coefficient appear to have a notable impact on the results.

Acknowledgments

This work was financially supported by the project "Synfuel" (4106-00006B) from the Innovation Fund Denmark. The PF code and the 3D visualization of the results were realized thanks to the financial support of the "the allianCe for ImagiNg of Energy MAterials", DSF-grant no. 1305-0032B via "The Danish Council for Strategic Research". Moreover, the authors would like to thank Jacob R. Bowen, Shenglan Yang, William Back Andrews, and Mujan Seif for their technical support. Finally, we acknowledge the support by the United States National Science Foundation, Division of Material Research, Ceramics Program, under the grant numbers DMR-1506055 and DMR-1912151.

References

[1] A. B. Stambouli, E. Traversa, Solid oxide fuel cells (SOFCs): a review of an environmentally clean and efficient source of energy, *Renewable and Sustainable Energy Reviews* 6, 433–455, 2002.

[2] W.Z. Zhu, S.C. Deevi, A review on the status of anode materials for solid oxide fuel cells, *Materials Science and Engineering A362*, 228–239, 2003.

[3] A. Ioselevich, Degradation of Solid Oxide Fuel Cell Anodes Due to Sintering of Metal Particles, *J. Electrochem. Soc. Vol. 144*, No. 9, 1997.

[4] S. P. Jiang, Sintering behavior of Ni/Y2O3-ZrO2 cermet electrodes of solid oxide fuel cells, *Journal of Materials Science 38*, 3775 – 3782, 2003.

[5] D. Simwonis, F. Tietz, D. Stöver, Nickel coarsening in annealed Ni/8YSZ anode substrates for solid oxide fuel cells, *Solid State Ionics 132, 241–251*, 2000.

[6] J. R. Wilson, W. Kobsiriphat, R. Mendoza, H.-Y. Chen, J. M. Hiller, D. J. Miller, K. Thornton, P. W. Voorhees, S. B. Adler, and S. A. Barnett, Three-dimensional reconstruction of a solid-oxide fuel-cell anode, *Nature Materials Vol 5*, 541-544, 2006.

[7] M. Trini, A. Hauch, S. De Angelis, X. Tong, P. Vang Hendriksen, M. Chen, Comparison of microstructural evolution of fuel electrodes in solid oxide fuel cells and electrolysis cells, *Journal of Power Sources 450*, 227599, 2020.

[8] D. Kennouche, Y. K. Chen-Wiegart, C. Riscoe, J. Wang, S. A. Barnett, Combined electrochemical and X-ray tomography study of the high temperature evolution of Nickel - Yttria Stabilized Zirconia solid oxide fuel cell anodes, *Journal of Power Sources 307*, 604-612, 2016.

[9] R. Vaßen, D. Simwonis, D. Stöver, Modelling of the agglomeration of Ni-particles in anodes of solid oxide fuel cells, *Journal of Materials Science 36*, 147– 151, 2001.

[10] S. Gao, J. Li, Z. Lin, Theoretical model for surface diffusion driven Ni-particle agglomeration in anode of solid oxide fuel cell, *Journal of Power Sources 255*, 144-150, 2014.

[11] A. Faes, A. Hessler-Wyser, D. Presvytes, C.G. Vayenas, J. Van herle, Nickel–Zirconia Anode Degradation and Triple Phase Boundary Quantification From Microstructural Analysis, *Fuel Cells 09*, No. 6, 841–851, 2009

[12] H.-Y. Chen, H.-C. Yu, J. Scott Cronin, J. R. Wilson, S. A. Barnett, K. Thornton, Simulation of coarsening in three-phase solid oxide fuel cell anodes, *Journal of Power Sources 196*, 1333–1337, 2011.

[13] Z. Jiao, and N. Shikazono, Simulation of Solid Oxide Fuel Cell Anode Microstructure Evolution Using Phase Field Method, *Journal of The Electrochemical Society 160 (6)*, F709-F715, 2013.

[14] Z. Jiao, and N. Shikazono, Simulation of Nickel Morphological and Crystal Structures Evolution in Solid Oxide Fuel Cell Anode Using Phase Field Method, *Journal of The Electrochemical Society 161 (5)*, F577-F582, 2014.

[15] Y. Lei, T.-L. Cheng, Y.-H. Wen, Phase field modeling of microstructure evolution and concomitant effective conductivity change in solid oxide fuel cell electrodes, *Journal of Power Sources 345*, 275-289, 2017.

[16] R. Davis, F. Abdeljawad, J. Lillibridge, M. Haataja, Phase wettability and microstructural evolution in solid oxide fuel cell anode materials, *Acta Materialia 78*, 271–281, 2014.

[17] Y. Lei, T.-L. Cheng, and Y.-H. Wen, Linking Initial Microstructure to Microstructure Evolution and Conductivity Change in SOFC Electrodes: A Phase Field Simulation, *ECS Transactions 78 (1)*, 2723-2739, 2017.

[18] K. Thydén, Y.L. Liu, J.B. Bilde-Sørensen, Microstructural characterization of SOFC Ni–YSZ anode composites by low-voltage scanning electron microscopy, *Solid State Ionics 178*, 1984–1989, 2008.

[19] A. Hauch, S. D. Ebbesen, S. H. Jensen, and M. Mogensen, Solid Oxide Electrolysis Cells: Microstructure and Degradation of the Ni/Yttria-Stabilized Zirconia Electrode, *Journal of The Electrochemical Society 155 (11)*, B1184-B1193, 2008.

[20] J. R. Izzo, Jr. Abhijit, S. Joshi, K. N. Grew, W. K. S. Chiu, A. Tkachuk, S. H. Wang, and W. Yunb, Nondestructive Reconstruction and Analysis of SOFC Anodes Using X-ray Computed Tomography at Sub-50 nm Resolution, *Journal of The Electrochemical Society 155 (5)*, B504-B508, 2008.

[21] J. Laurencin, R. Quey, G. Delette, H. Suhonen, P. Cloetens, P. Bleuet, Characterisation of Solid Oxide Fuel Cell Ni–8YSZ substrate by synchrotron X-ray nano-tomography: from 3D reconstruction to microstructure quantification, *Journal of Power Sources 198*, 182– 189, 2012.

[22] Y. C. K. Chen-Wiegart, J. S. Cronin, Q. Yuan, K. J. Yakal-Kremski, S. A. Barnett, J. Wang, 3D Non-destructive morphological analysis of a solid oxide fuel cell anode using full-field X-ray nano-tomography, *Journal of Power Sources 218*, 348-351, 2012.

[23] J. S. Cronin, Y. C. K. Chen-Wiegart, J. Wang, S. A. Barnett, Three-dimensional reconstruction and analysis of an entire solid oxide fuel cell by full-field transmission X-ray microscopy, *Journal of Power Sources 233*, 174-179, 2013.

[24] S. De Angelis, P. S. Jørgensen, V. Esposito, E. H. R. Tsai, M. Holler, K. Kreka, E. Abdellahi, J. R. Bowen, Ex-situ tracking solid oxide cell electrode microstructural evolution in a redox cycle by high resolution ptychographic nanotomography, *Journal of Power Sources 360*, 520-527, 2017.

[25] S. De Angelis, P. S. Jørgensen, E. H. R. Tsai, M. Holler, K. Kreka, J. R. Bowen, Three dimensional characterization of nickel coarsening in solid oxide cells via ex-situ ptychographic nano-tomography, *Journal of Power Sources 383*, 72–79, 2018.

[26] B. Münch, and L. Holzer, Contradicting Geometrical Concepts in Pore Size Analysis Attained with Electron Microscopy and Mercury Intrusion, *J. Am. Ceram. Soc., 91 (12)*, 4059–4067 (2008), 2008.

[27] P.R. Shearing, J. Gelb, J. Yi, W.-K. Lee, M. Drakopolous, N.P. Brandon, Analysis of triple phase contact in Ni–YSZ microstructures using non-destructive X-ray tomography with synchrotron radiation, *Electrochemistry Communications 12*, 1021–1024, 2010.

[28] P. S. Jørgensen, S. L. Ebbehøj, A. Hauch, Triple phase boundary specific pathway analysis for quantitative characterization of solid oxide cell electrode microstructure, *Journal of Power Sources 279*, 686-693, 2015.

[29] S. L. Ebbehøj, T. Ramos, and M. Mogensen, Impact of Reduction Parameters on the Initial Performance and Stability of Ni/(Sc)YSZ Cermet Anodes for SOFCs, *ECS Transactions 45 (1)*, 363-375, 2012.

[30] M. Holler, J. Raabe, A. Diaz, M. Guizar-Sicairos, C. Quitmann, A. Menzel, and O. Bunk, An instrument for 3D x-ray nano-imaging, *Rev. Sci. Instrum. 83*, 073703, 2012.

[31] P. J. Besl, and N. D. McKay, A Method for Registration of 3-D Shapes, *Proc. SPIE 1611, Sensor Fusion IV: Control Paradigms and Data Structures*, 1992.

692 [32] P.S. Jørgensen, K.V. Hansen, R. Larsen, J.R. Bowen, High accuracy interface characterization
693 of three phase material systems in three dimensions, *Journal of Power Sources 195*, 8168–8176, 2010

694 [33] R. Mendoza, J. Alkemper, and P. W. Voorhees, The Morphological Evolution of Dendritic
695 Microstructures during Coarsening, *Metallurgical and Materials Transactions A, Volume 34A*, 481
696 March 2003.

697 [34] C.-L. Park, P.W. Voorhees, K. Thornton, Application of the level-set method to the analysis of
698 an evolving microstructure, *Computational Materials Science 85*, 46–58, 2014.

699 [35] R. Mendoza, I. Savin, K. Thornton and P. W. Voorhees, Topological complexity and the
700 dynamics of coarsening, *Nature Materials Vol 3*, 385-388, June 2004.

701 [36] N. Moelans, B. Blanpain, P. Wollants, An introduction to phase-field modeling of microstructure
702 evolution, *Computer Coupling of Phase Diagrams and Thermochemistry 32*, 268–294, 2008.

703 [37] M. Irshad, K. Siraj, R. Raza, A. Ali, P. Tiwari, B. Zhu, A. Rafique, A. Ali, M. K. Ullah, and A.
704 Usman, A Brief Description of High Temperature Solid Oxide Fuel Cell's Operation, *Materials,*
705 *Design, Fabrication Technologies and Performance, Appl. Sci. 6*, 75, 2016.

706 [38] M. Trini, P. S. Jørgensen, A. Hauch, M. Chen, P. V. Hendriksen, Microstructural
707 Characterization of Ni/YSZ Electrodes in a Solid Oxide Electrolysis Stack Tested for 9000 Hours,
708 *ECS Transactions 78 (1),* 3049-3064, 2017.

709 [39] P. Tanasini, M. Cannarozzo, P. Costamagna, A. Faes, J. VanHerle, A. Hessler-Wyser, and C.
710 Comninellis, Experimental and Theoretical Investigation of Degradation Mechanisms by Particle
711 Coarsening in SOFC Electrodes, *Fuel Cells 09 No. 5*, 740–752, 2009.

712 [40] J. M. Blakely, and H. Mykura, Surface Self Diffusion Measurements On Nickel By The Mass
713 Transfer Method, *Acta Metallurgica Vol. 9*, 1961.

714 [41] V. L. Ginzburg, On Superconductivity and Superfluidity, A Scientific Autobiography, *Springer-*
715 *Verlag Berlin Heidelberg*, 2009.

716 [42] P.C. Hohenberg, and A.P. Krekhov, An introduction to the Ginzburg-Landau theory of phase
717 transitions and nonequilibrium patterns, *Phys. Rep. Vol. 572*, pp. 1-42, 2015.

718 [43] H.-C. Yu, H.-Y. Chen, and K. Thornton, Extended smoothed boundary method for solving partial
719 differential equations with general boundary conditions on complex boundaries, *Modelling Simul.*
720 *Mater. Sci. Eng. 20*, 075008 (41pp), 2012.

721 [44] R. J. LeVeque, Finite Difference Method for Ordinary and Partial Differential Equation, *The*
722 *Society for Industrial and Applied Mathematices*, 2007.

723 [45] A. Tsoga, A. Naoumidis and P. Nikolopoulos, Wettability And Interfacial Reactions In The
724 Systems Ni/YSZ and Ni/Ti-TiOz/YSZ, *Acra mater. Vol. 44. No. 9*, pp. 3679-3692, 1996.

725 [46] Y. K. Chen-Wiegart, D. Kennouche, J. S. Cronin, S. A. Barnett, and J. Wang, Effect of Ni content
726 on the morphological evolution of Ni-YSZ solid oxide fuel cell electrodes, *Applied Physics Letters*
727 *108*, 083903, 2016.

728 [47] B. Shri Prakashn, S. Senthil Kumar, S.T. Aruna, Properties and development of Ni/YSZ as an
729 anode material in solid oxide fuel cell: A review, *Renewable and Sustainable Energy Reviews 36*,
730 149–179, 2014

731 [48] D. Kennouche, Y. Karen Chen-Wiegart, J. S. Cronin, J. Wang, and Scott A. Barnett, Three-
732 Dimensional Microstructural Evolution of Ni-Yttria-Stabilized Zirconia Solid Oxide Fuel Cell
733 Anodes At Elevated Temperatures, *Journal of The Electrochemical Society 160 (11)*, F1293-F1304,
734 2013.

735 [49] Z. Jiao, N. Shikazono, Study on the effects of polarization on local morphological change of
736 nickel at active three-phase-boundary using patterned nickel-film electrode in solid oxide fuel cell
737 anode, *Acta Materialia 135*, 124-131, 2017.

738 [50] X. Mantzouris, N. Zouvelou, D. Skarmoutsos, P. Nikolopoulos, F. Tietz, Interfacial properties
739 and structure stability of Ni/Y_2O_3-ZrO_2-TiO_2 cermet anodes for solid oxide fuel cells, *J. Mater. Sci.*,
740 40, 2471-2475, 2005.

741 [51] J. Hektor, S. A. Hall, N. A. Henningsson, J. Engqvist, M. Ristinmaa, F. Lenrick, and J. P. Wright,
742 Scanning 3DXRD Measurement of Grain Growth, Stress, and Formation of Cu_6Sn_5 around a Tin
743 Whisker during Heat Treatment, *Materials 12*, 446, 2019.

744 [52] James R. Wilson, Marcio Gameiro, Konstantin Mischaikow, William Kalies, Peter W. Voorhees
745 and Scott A. Barnett,Three-Dimensional Analysis of Solid Oxide Fuel Cell Ni-YSZ Anode
746 Interconnectivity, Microscopy and Microanalysis, 15, 1, 71-77, 2009.

747